

Analytic Morse/long-range potential energy surfaces and “adiabatic-hindered-rotor” treatment for a symmetric top-linear molecule dimer: A case study of CH₃F–H₂

Cite as: J. Chem. Phys. **148**, 124302 (2018); <https://doi.org/10.1063/1.5024451>

Submitted: 01 February 2018 . Accepted: 06 March 2018 . Published Online: 22 March 2018

Xiao-Long Zhang , Yong-Tao Ma, Yu Zhai , and Hui Li 



View Online



Export Citation



CrossMark

ARTICLES YOU MAY BE INTERESTED IN

Explicit correlation treatment of the six-dimensional potential energy surface and predicted infrared spectra for OCS–H₂

The Journal of Chemical Physics **147**, 044313 (2017); <https://doi.org/10.1063/1.4996086>

The Role of High Excitations in Constructing Sub-spectroscopic Accuracy Intermolecular Potential of He–HCN: Critically Examined by the High-Resolution Spectra with Resonance States

Chinese Journal of Chemical Physics **30**, 776 (2017); <https://doi.org/10.1063/1.674-0068/30/cjcp1712231>

A full-dimensional potential energy surface and quantum dynamics of inelastic collision process for H₂–HF

The Journal of Chemical Physics **148**, 184301 (2018); <https://doi.org/10.1063/1.5030384>

PHYSICS TODAY
WHITEPAPERS

ADVANCED LIGHT CURE ADHESIVES

Take a closer look at what these environmentally friendly adhesive systems can do

READ NOW

PRESENTED BY
MASTERBOND
ADHESIVES | SEALANTS | COATINGS

Analytic Morse/long-range potential energy surfaces and “adiabatic-hindered-rotor” treatment for a symmetric top-linear molecule dimer: A case study of CH₃F–H₂

Xiao-Long Zhang, Yong-Tao Ma, Yu Zhai, and Hui Li^{a)}

Laboratory of Theoretical and Computational Chemistry, Institute of Theoretical Chemistry, Jilin University, 2519 Jiefang Road, Changchun 130023, People's Republic of China

(Received 1 February 2018; accepted 6 March 2018; published online 22 March 2018)

A first effective six-dimensional *ab initio* potential energy surface (PES) for CH₃F–H₂ which explicitly includes the intramolecular Q₃ stretching normal mode of the CH₃F monomer is presented. The electronic structure computations have been carried out at the explicitly correlated coupled cluster level of theory [CCSD(T)-F12a] with an augmented correlation-consistent triple zeta basis set. Five-dimensional analytical intermolecular PESs for $\nu_3(\text{CH}_3\text{F}) = 0$ and 1 are then obtained by fitting the vibrationally averaged potentials to the Morse/Long-Range (MLR) potential function form. The MLR function form is applied to the nonlinear molecule-linear molecule case for the first time. These fits to 25 015 points have root-mean-square deviations of 0.74 cm^{−1} and 0.082 cm^{−1} for interaction energies less than 0.0 cm^{−1}. Using the adiabatic hindered-rotor approximation, three-dimensional PESs for CH₃F–*para*H₂ are generated from the 5D PESs over all possible orientations of the hydrogen monomer. The infrared and microwave spectra for CH₃F–*para*H₂ dimer are predicted for the first time. These analytic PESs can be used for modeling the dynamical behavior in CH₃F–(H₂)_N clusters, including the possible appearance of microscopic superfluidity. *Published by AIP Publishing.* <https://doi.org/10.1063/1.5024451>

I. INTRODUCTION

Solid hydrogen is a molecular quantum crystal; the emergent use of solid hydrogen as a matrix host for spectroscopic studies is of fundamental interest because of its unusual properties.¹ Solid parahydrogen (*p*H₂) having zero nuclear spin angular momentum is especially attractive in matrix isolation spectroscopy^{2–4} since the spherical symmetry of the rotational wavefunction of *p*H₂ causes all permanent electric multipole moments to vanish and thus its electrostatic character is spherical as in rare gas atoms. Accordingly, spectra of many molecules isolated in solid *p*H₂ have now been studied.^{5–7} Moreover, a fine structure is observable because the infrared (IR) absorption lines of guest molecules in the *p*H₂ matrix are extremely narrow.^{8,9}

In solid *p*H₂, CH₃F and CH₃F–(*ortho*-H₂)_n have been well studied by Fourier-transform infrared (FTIR)^{10–13} and laser absorption spectroscopy^{14–18} as an example of weakly bound clusters containing a polar symmetric top. However, there are still many unanswered and intriguing questions raised concerning CH₃F in the solid *p*H₂ system.¹⁵ An understanding of the experimental spectra at the microscopic scale requires complementary computer simulation studies based on accurate intermolecular potential energy functions. Unfortunately, to our knowledge, the potential energy surfaces (PESs) and rovibrational spectra of the CH₃F–H₂ dimer have not been reported up to now. This inspired us to construct

a high level *ab initio* PES for CH₃F–H₂ which explicitly incorporates the Q₃ symmetric-stretch vibrational motion of CH₃F.

Many calculations for the rovibrational spectra of the polyatomic-polyatomic dimers^{19–25} and collisions^{26,27} strongly depend on their highly accurate PESs. The reliable potential function models are of great importance for performing the fit to intermolecular potentials. In recent years, some interpolation schemes have been largely employed to describe the intermolecular potentials for the nonlinear molecule-linear molecule case, in which the PES can be expanded into a series of appropriate angular functions multiplied by radial coefficients.^{28,29} However, such interpolation cannot perform a global fitting. Recently, Le Roy *et al.* introduced the Morse/Long-Range (MLR) radial potential function form which incorporates theoretically known long-range inverse-power behavior within a single smooth and flexible analytic function.^{30,31} For atom-molecule or molecule-molecule systems, allowing parameters of that radial function to vary with angle and monomer-stretching coordinate yields a compact and flexible multi-dimensional functional form. This flexible global function form has been successfully used for atom-atom,³² linear molecule-atom,^{33,34} linear molecule-linear molecule,^{35–39} and nonlinear molecule-atom cases.^{40,41} In this paper, we extend this model for the more challenging nonlinear molecule-linear molecule case such as the CH₃F–H₂ system for the first time.

To provide a proper understanding of the dynamical behavior in CH₃F–(H₂)_N clusters and *p*H₂ matrix isolated CH₃F, including the possible appearance of superfluidity

^{a)}E-mail: Prof.huili@jlu.edu.cn

and quantitative study of the evolution of the ν_3 vibrational band-origin shift with increase in the cluster size N , an accurate description of the C–F symmetric stretching mode for the dimer PES is essential. However, taking full account of the rotational degree of freedom of H_2 would dramatically increase the computational cost of cluster simulations. Thus providing an accurate reduced-dimensional treatment of the orientations of H_2 is very desirable. In the present work, 5D versions (depending on four angles and R) of MLR functions have been fitted to vibrationally averaged interaction energies obtained from a new six-dimensional (6D) *ab initio* PES for $\text{CH}_3\text{F}-\text{H}_2$ which explicitly incorporate the stretch vibrational motion of C–F. Afterwards, an adiabatic-hindered-rotor (AHR) approximation^{42,43} was applied to the $\text{CH}_3\text{F}-\text{H}_2$ system; this approximation would remove the two angles that describe the relative orientation of the rigid H_2 , and the 5D PESs would be reduced to new 3D adiabatic effective PESs. Energies and wave functions of the discrete rovibrational levels of $\text{CH}_3\text{F}-p\text{H}_2$ complexes are obtained from the adiabatic 3D potentials and compared with the previous $\text{CH}_3\text{F}-\text{Rg}$ (He, Ne, Ar) complex.

This paper is arranged as follows. The new *ab initio* calculations, analytic potential function form, and fitting parameters are described in Sec. II. Section III then presents the AHR treatment and compares the features of the previous $\text{CH}_3\text{F}-\text{He}$ complex. Section IV presents predictions of the infrared and microwave (MW) spectra for the $\text{CH}_3\text{F}-p\text{H}_2$ dimer. Discussion and conclusions are given in Sec. IV.

II. COMPUTATIONAL DETAILS

A. *Ab initio* calculations

The body-fixed coordinates ($R, \theta_1, \theta_2, \phi_1, \phi_2, Q_3$) used in this work are shown in Fig. 1(a). The origin of coordinates coincides with the center of mass of the CH_3F molecule with the z -axis being its threefold symmetry axis. One of the hydrogen atoms of the CH_3F molecule lies in the xz -plane. The intermolecular vector \mathbf{R} connects the center of mass of CH_3F and H_2 molecules. The angles θ_1 and ϕ_1 describe the orientation of vector \mathbf{R} with respect to the CH_3F molecule (body-fixed frame 1). The rotation of the H_2 molecule relative to frame 2, which is parallel to body-fixed frame 1, is defined by θ_2 and ϕ_2 angles. Q_3 is the normal mode coordinate of the ν_3 vibration for the CH_3F molecule.

For the *ab initio* calculations, the bond length of the H_2 molecule was fixed at the average value for the ground

state $\langle r \rangle = 0.7666393 \text{ \AA}$,⁴⁴ and the geometry of CH_3F molecule is the same as in our previous paper,⁴¹ which gives a good agreement of theoretical predictions with experiment. The six-dimensional (6D) PES of the $\text{CH}_3\text{F}-\text{H}_2$ complex was carried out at the explicitly correlated coupled cluster with single, double, and perturbative triple excitations [CCSD(T)]-F12a⁴⁵ level of theory with an augmented correlation-consistent triple zeta (aVTZ) basis set⁴⁶ using the MOLPRO package.⁴⁷ The full counterpoise procedure was employed to correct for the basis set superposition error (BSSE).⁴⁸

In the preparation of the 6D PES $\Delta V(R, \theta_1, \theta_2, \phi_1, \phi_2, Q_3; Q_m)$, a total of $5 \times 25\,015$ *ab initio* points with energies smaller than 2000 cm^{-1} were calculated. The calculations were performed on regular grids for all six degrees of freedom. Five potential optimized discrete variable representation (PODVR)^{49,50} grid points corresponding to $Q_3 = -0.2922, -0.1581, -0.0422, 0.0690$, and 0.1868 \AA were used with other normal mode Q_m ($m = 1, 2, 4, 5, 6$) coordinates fixed at the vibrational averaged values, while a relatively dense grid of 15 points ranging from 2.4 to 9.0 \AA was used for the R intermolecular coordinate. The angular coordinates θ_1 and θ_2 range from 0 to 180° with step sizes of 15° , and the dihedral angle ϕ_1 ranges from 0 to 60° at intervals of 30° due to the C_{3v} symmetry of CH_3F . Similarly, due to the symmetry of H_2 , the dihedral angle ϕ_2 ranges from 0 to 180° at intervals of 30° while $\phi_1 = 30$ or 60° , and the ϕ_2 only ranges from 0 to 180° at intervals of 30° .

Within the Born-Oppenheimer approximation, the treatment of the inter- and intra-molecular motions is separated because the vibration of CH_3F has a much higher frequency than the intermolecular motions. The total vibrational wave function can be written as the product,

$$\Psi_{\nu_3}(R, \theta_1, \theta_2, \phi_1, \phi_2, Q_3; Q_m) = \phi_{\nu_3}(R, \theta_1, \theta_2, \phi_1, \phi_2) \psi_{\nu_3}(Q_3; Q_m), \quad (1)$$

in which ν_3 is the quantum number for a specific stretching vibrational state of the free CH_3F molecule and the wavefunction $\psi_{\nu_3}(Q_3; Q_m)$ is obtained by solving the 1D Schrödinger equation

$$\left[\frac{-1}{2M} \frac{d^2}{dQ_3^2} + V_{\text{CH}_3\text{F}}(Q_3; Q_m) \right] \psi_{\nu_3}(Q_3; Q_m) = E_{\nu_3} \psi_{\nu_3}(Q_3; Q_m), \quad (2)$$

where $V_{\text{CH}_3\text{F}}(Q_3; Q_m)$ is the intramolecular potential of the isolated CH_3F molecule and M is the reduced mass of the

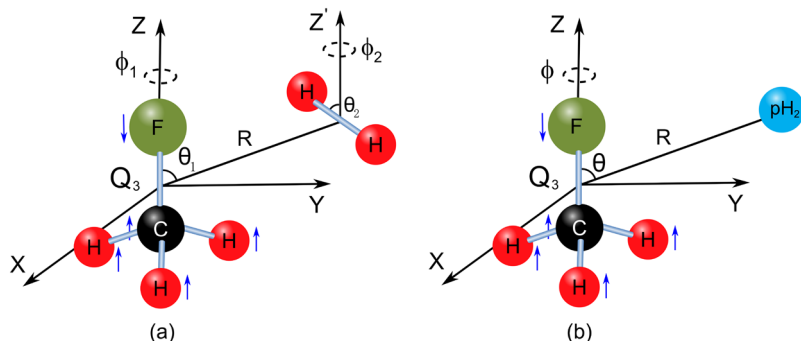


FIG. 1. (a) Coordinate systems used to describe the interaction between CH_3F and H_2 and (b) frames used to generate the AHR effective 3D PES for $\text{CH}_3\text{F}-p\text{H}_2$.

C–F symmetric stretching mode of the CH₃F molecule. Using Eq. (1), the vibrationally averaged CH₃F–H₂ interaction potential for CH₃F in ground ($\nu_3 = 0$) and first excited ($\nu_3 = 1$) states are written as

$$\begin{aligned} \bar{V}_{[\nu_3]}(R, \theta_1, \theta_2, \phi_1, \phi_2) = & \int_{-\infty}^{\infty} \psi_{\nu_3}^*(Q_3; Q_m) \Delta V \\ & \times (R, \theta_1, \theta_2, \phi_1, \phi_2, Q_3; Q_m) \\ & \times \psi_{\nu_3}(Q_3; Q_m) dQ_3. \end{aligned} \quad (3)$$

B. Analytic potential energy function

Our vibrationally averaged *ab initio* intermolecular potential energies $\bar{V}_{[\nu_3]}(R, \theta_1, \theta_2, \phi_1, \phi_2)$ for the CH₃F–H₂ were fitted to a five-dimensional MLR potential function,^{32,51} which is written as

$$\begin{aligned} \bar{V}_{\text{MLR}}(R, \Omega) = & \mathfrak{D}_e(\Omega) \\ & \times \left\{ -1 + \left[1 - \frac{u_{\text{LR}}(R, \Omega)}{u_{\text{LR}}(R_e, \Omega)} e^{-\beta(R, \Omega) \cdot y_p^{\text{eq}}(R, \Omega)} \right]^2 \right\} \\ & + \bar{V}_{\text{elst}}(R, \Omega), \end{aligned} \quad (4)$$

in which $\Omega \equiv (\theta_1, \theta_2, \phi_1, \phi_2)$ and $\bar{V}_{\text{elst}}(R, \Omega)$ is the electrostatic interaction. The leading terms are the dipole-quadrupole and quadrupole-quadrupole interactions, which are given by

$$\bar{V}_{\text{elst}}(R, \Omega) = \frac{\bar{C}_4(\Omega)}{R^4} + \frac{\bar{C}_5(\Omega)}{R^5}, \quad (5)$$

$\mathfrak{D}_e(\Omega)$ and $R_e(\Omega)$ are the depth and position of the minimum on a radial cut through the potential for angles Ω , respectively, while $u_{\text{LR}}(R, \Omega)$ is a function which defines the (attractive) limiting long-range behavior of the effective 1D potential along that cut as

$$u_{\text{LR}}(R, \Omega) = \frac{\bar{C}_6(\Omega)}{R^6} + \frac{\bar{C}_7(\Omega)}{R^7} + \frac{\bar{C}_8(\Omega)}{R^8}, \quad (6)$$

in which the long range coefficients \bar{C}_n have also been averaged over the CH₃F ν_3 vibration coordinate Q_3 , and the denominator factor $u_{\text{LR}}(R_e, \Omega)$ is that same function evaluated at $R = R_e(\Omega)$.

The radial distance variable in the exponent in Eq. (4) is the dimensionless quantity

$$y_p^{\text{eq}}(R, \Omega) = \frac{R^p - R_e(\Omega)^p}{R^p + R_e(\Omega)^p}, \quad (7)$$

where p is a small positive integer which must be greater than the difference between the largest and smallest (inverse) powers appearing in Eq. (6), $p > (8 - 6)$,⁵¹ and the exponent coefficient function $\beta(R, \Omega)$ is a (fairly) slowly varying function of R , which is written as the constrained polynomial

$$\begin{aligned} \beta(R, \Omega) = & y_p^{\text{ref}}(R, \Omega) \beta_{\infty}(\Omega) \\ & + [1 - y_p^{\text{ref}}(R, \Omega)] \sum_{i=0}^N \beta_i(\Omega) y_q^{\text{ref}}(R, \Omega)^i, \end{aligned} \quad (8)$$

whose behaviour is defined in terms of the two new radial variables

$$y_p^{\text{ref}}(R, \Omega) = \frac{R^p - R_{\text{ref}}^p}{R^p + R_{\text{ref}}^p} \text{ and } y_q^{\text{ref}}(R, \Omega) = \frac{R^q - R_{\text{ref}}^q}{R^q + R_{\text{ref}}^q}, \quad (9)$$

in which $R_{\text{ref}} \equiv f_{\text{ref}} \times R_e(\Omega)$. In the present work of the potential function model, $p = 3$, $q = 2$, and $f_{\text{ref}} = 1.0$.

The definition of $y_p^{\text{eq}}(R, \Omega)$ and the algebraic structure of Eqs. (4) and (8) mean that

$$\begin{aligned} \lim_{R \rightarrow \infty} \beta(R, \Omega) &= \lim_{R \rightarrow \infty} \{\beta(R, \Omega) \cdot y_p^{\text{eq}}(R, \Omega)\} \\ &= \beta_{\infty}(\Omega) \\ &= \ln\{2 \mathfrak{D}_e(\Omega) / u_{\text{LR}}(R_e, \Omega)\}. \end{aligned} \quad (10)$$

The parameters $\mathfrak{D}_e(\Omega)$ and $R_e(\Omega)$ and the various exponent expansion coefficients $\beta_i(\Omega)$ are all expanded in the form

$$F(\Omega) = \sum_{l_1 m_1 l_2 l} F_{l_1 m_1 l_2 l} t_{l_1 m_1 l_2 l}(\Omega), \quad (11)$$

in which $F = \mathfrak{D}_e, R_e$, or β_i and where the functions $t_{l_1 m_1 l_2 l}(\Omega)$ are explicitly given in the works of Phillips *et al.*²⁸ and Valiron *et al.*,²⁹

$$\begin{aligned} t_{l_1 m_1 l_2 l}(\Omega) = & [2(1 + \delta_{m_{10}})^{-1} (2l_1 + 1)^{-1}]^{-\frac{1}{2}} (1 + \delta_{m_{10}})^{-1} \\ & \times \sum_{r_1 r_2} \begin{pmatrix} l_1 & l_2 & l \\ r_1 & r_2 & r \end{pmatrix} Y_{l_2 r_2}(\theta_2, \phi_2) Y_{l r}(\theta_1, \phi_1) \\ & \times [\delta_{m_1 r_1} + (-1)^{l_1 + m_1 + l_2 + l} \delta_{-m_1 r_1}]. \end{aligned} \quad (12)$$

The indices l_1 , l_2 , and l refer to the tensor rank of the angle dependence of the CH₃F orientation, the H₂ orientation, and the intermolecular vector orientation, respectively. The l has the range of values $|l_1 - l_2| \leq l \leq |l_1 + l_2|$. These three indices must satisfy the restrictions that $l_1 + l_2 + l$ is even and l_2 is also even due to the symmetry of H₂. In the rigid rotor approximation, the C_{3v} symmetry of CH₃F further restricts that m_1 is a multiple of 3.

The presence of a permanent dipole on CH₃F and quadrupole moments on CH₃F and H₂ means that the leading terms in the expression for $u_{\text{LR}}(R, \Omega)$ are the electrostatic dipole-quadrupole and quadrupole-quadrupole interaction, whose (vibrationally averaged) coefficient may be written as

$$\bar{C}_4(\Omega) = -(\sqrt{105}) \bar{\mu}_{\text{CH}_3\text{F}} \bar{Q}_{\text{H}_2} t_{1023}(\Omega), \quad (13)$$

$$\bar{C}_5(\Omega) = -(3\sqrt{70}) \bar{Q}_{\text{CH}_3\text{F}} \bar{Q}_{\text{H}_2} t_{2024}(\Omega), \quad (14)$$

in which $\bar{\mu}_{\text{CH}_3\text{F}}$ and $\bar{Q}_{\text{CH}_3\text{F}}$ and \bar{Q}_{H_2} are the vibrationally averaged dipole and quadrupole moments of CH₃F and H₂, respectively.

The long-range \bar{C}_6 coefficients $\bar{C}_6 = \bar{C}_{6,\text{ind}} + \bar{C}_{6,\text{disp}}$, where $\bar{C}_{6,\text{disp}}$ and $\bar{C}_{6,\text{ind}}$ refer to dispersion and induction force coefficients. The vibrational ground state coefficient $\bar{C}_{6,\text{disp}}$ is obtained from formula (14) of Ref. 52. While the long-range vibrationally excited states $\bar{C}_{6,\text{disp}}^{\nu_3}$ are estimated from

$$\bar{C}_{6,\text{disp}}^{\nu_3=1} \cong \frac{\bar{\alpha}_{\text{CH}_3\text{F}}^{\nu_3=1}}{\bar{\alpha}_{\text{CH}_3\text{F}}^{\nu_3=0}} \times \bar{C}_{6,\text{disp}}^{\nu_3=0}, \quad (15)$$

the $\bar{C}_{6,\text{ind}}$ are calculated in the form

$$\bar{C}_{6,\text{ind}} = \langle \mu_{\text{CH}_3\text{F}}^2 \rangle \alpha_{\text{H}_2}. \quad (16)$$

In Eqs. (15) and (16), $\mu_{\text{CH}_3\text{F}}$ and $\alpha_{\text{CH}_3\text{F}}$ are the dipole moment and polarizability of the CH_3F molecule which is obtained at the CCSD(T)/aug-cc-pVQZ level using the finite-field method,^{53,54} while α_{H_2} is the polarizability of atom H_2 .⁵⁵ The vibrationally averaged long-range coefficients $\bar{C}_{6(7,8)}(\Omega)$ are expanded as

$$\bar{C}_{6(7,8)}(\Omega) = \sum \bar{C}_{6(7,8)}^{l_1 m_1 l_2 l} t_{l_1 m_1 l_2 l}(\Omega).$$

As discussed above, the leading vibrationally averaged isotropic coefficient \bar{C}_6^{0000} has been obtained. However, no angle or stretching-dependent long-range coefficients have been reported for this system. In this work, once we obtained the leading vibrationally averaged coefficient \bar{C}_6^{0000} , the other angle dependent term $\bar{C}_{6(7,8)}^{l_1 m_1 l_2 l}$ was then obtained by fitting the vibrationally averaged intermolecular potentials with $R \geq 6$ to Eq. (6).

C. Least-squares fits

Realistic initial trial values of the fitting parameters are essential to commence the non-linear least-squares fit, and they were obtained as follows. First, the radial R depending energies are fitted to the ordinary 1D MLR form for all distinct combinations of (Ω) using program betaFIT.⁵⁶ The resulting values of $\mathfrak{D}_e(\Omega)$, $R_e(\Omega)$, and $\beta_i(\Omega)$ (for $i = 0 - N$) were then fitted to Eq. (11), and the resulting expansion coefficients were used as initial trial parameters in the global 5D fits of the vibrationally averaged potential energies to Eq. (4).

In the final 5D fits, the input *ab initio* energies were weighted by assigning uncertainties of $u_i = 0.1 \text{ cm}^{-1}$ to points in the attractive well region where $V(R, \Omega) \leq 0.0 \text{ cm}^{-1}$ and $u_i = [V(R, \theta_1, \theta_2, \phi) + 5.0]/50.0 \text{ cm}^{-1}$ to those in the repulsive wall region where $V(R, \Omega) > 0.0 \text{ cm}^{-1}$. Using these weights, our final 823 parameter fits to the 25 015 vibrationally averaged interaction energies for $\bar{V}(R, \Omega) < 2000 \text{ cm}^{-1}$ yielded dimensionless root-mean-square (RMS) residual discrepancies of only 0.74 cm^{-1} and 0.082 cm^{-1} in the van der Waals minimum region of the interaction. More than 232 of those fitting parameters are required to define $\mathfrak{D}_e(\Omega)$, 232 to define $R_e(\Omega)$, and 232 and 126 to define $\beta_i(\Omega)$ for $i = 0, 1$, respectively. At the

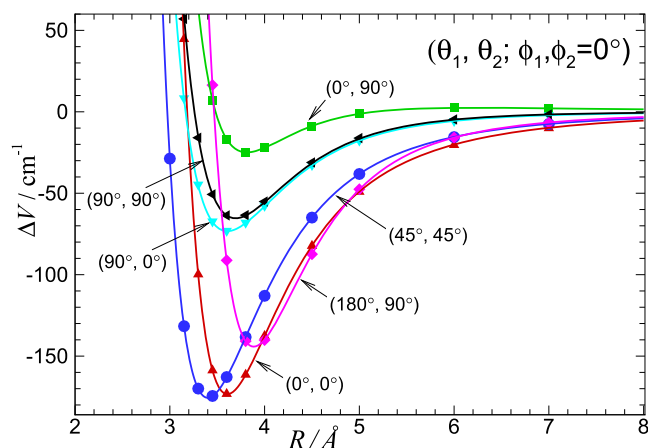


FIG. 2. *Ab initio* energies (points) compared with the analytic 5D V_{MLR} PES for $\text{CH}_3\text{F}-\text{H}_2$ at various relative orientations.

resolution of Fig. 2, the resulting fitted potential passes through all of the (vibrationally averaged) *ab initio* points shown. The resulting sets of potential parameters and a FORTRAN subroutine for generating these potentials may be obtained from the authors or from the journal's supplementary data archive.

D. Adiabatic hindered-rotor treatment of the rotation of H_2

Within the Born-Oppenheimer approximation, the rovibrational Hamiltonian of the $\text{CH}_3\text{F}-\text{H}_2$ complex in the Jacobi coordinate system can be written as⁵⁷⁻⁶⁰

$$\hat{H} = -\frac{\hbar^2}{2\mu} \frac{\partial^2}{\partial R^2} + \frac{(\hat{J} - \hat{j}_1 - \hat{j}_2)^2}{2\mu R^2} + \hat{T}_{\text{CH}_3\text{F}} + \hat{T}_{\text{H}_2} + \Delta\bar{V}(R, \theta_1, \theta_2, \phi_1, \phi_2), \quad (17)$$

in which \hat{J} is the total angular momentum operator for the whole dimer; \hat{j}_1 and \hat{j}_2 are the angular momentum operators of CH_3F and H_2 , respectively; μ is the reduced mass of the dimer; $\Delta\bar{V}$ is the intermolecular potential; and $\hat{T}_{\text{CH}_3\text{F}}$ stands for the rigid rotor kinetic energy operator of the CH_3F monomer,

$$\hat{T}_{\text{CH}_3\text{F}} = B\hat{j}^2 + (A - B)\hat{j}_z^2 - D_J\hat{j}^4 - D_{JK}\hat{j}^2\hat{j}_z^2 - D_K\hat{j}_z^4, \quad (18)$$

where the rotational constants (A and B) and the quadric centrifugal distortion coefficients (D_J , D_{JK} , and D_K) for CH_3F were taken from experimental data.^{61,62}

The inertial rotational constant for $p\text{H}_2$ (59.322 cm^{-1}) is more than 11 times larger than the A (5.182 cm^{-1}) of the CH_3F molecule and 70 times larger than its B (0.852 cm^{-1}). Thus, following the approach of Li and co-workers,^{42,43} a Born-Oppenheimer type separation of H_2 -rotation from the other motions could be performed to generate an effective potential depending only on the three polar coordinates θ_1 , ϕ_1 , and R which determine the position of a point-like $p\text{H}_2$ relative to the CH_3F . In this “adiabatic hindered-rotor” treatment, a

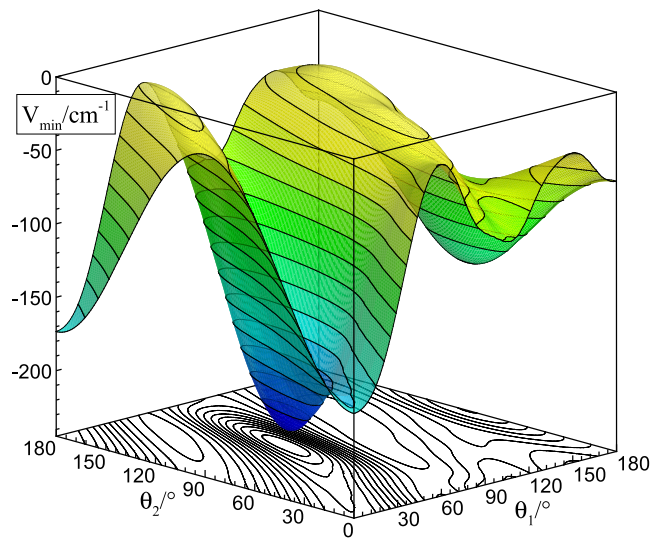


FIG. 3. Minimum energy on our vibrationally averaged 5D V_{MLR} PES for $\text{CH}_3\text{F}(v_3=0)-\text{H}_2$ as a function of angles θ_1 and θ_2 with ϕ_1 and ϕ_2 fixed at their equilibrium values corresponding to the global minimum, for the optimized value of R .

$p\text{H}_2$ located at any (R, θ_1, ϕ_1) position relative to the CH_3F molecule is treated as a hindered rotor subject to the three-dimensional angular potential $V_{\nu_3}(\theta_2, \phi_2; R, \theta_1, \phi_1)$. For any particular (R, θ_1, ϕ_1) configuration, the H_2 adiabatic state is determined by

$$\hat{H}_{\text{H}_2}(\theta_2, \phi_2; R, \theta_1, \phi_1)\Psi(\theta_2, \phi_2; R, \theta_1, \phi_1) = E_{\text{H}_2}(R, \theta_1, \phi_1)\Psi(\theta_2, \phi_2; R, \theta_1, \phi_1), \quad (19)$$

with

$$\hat{H}_{\text{H}_2}(\theta_2, \phi_2; R, \theta_1, \phi_1) = B_{\text{H}_2}\hat{j}_2^2 + V_{\nu_3}(\theta_2, \phi_2; R, \theta_1, \phi_1). \quad (20)$$

Equation (19) can be solved using a basis set of spherical harmonic functions $Y_{lm}(\theta_2, \phi_2)$, and the lowest eigenvalues then define a 3D effective hindered-rotor PES

$$V^{\text{AHR}}(R, \theta, \phi) = E_{\text{H}_2}(R, \theta_1, \phi_1). \quad (21)$$

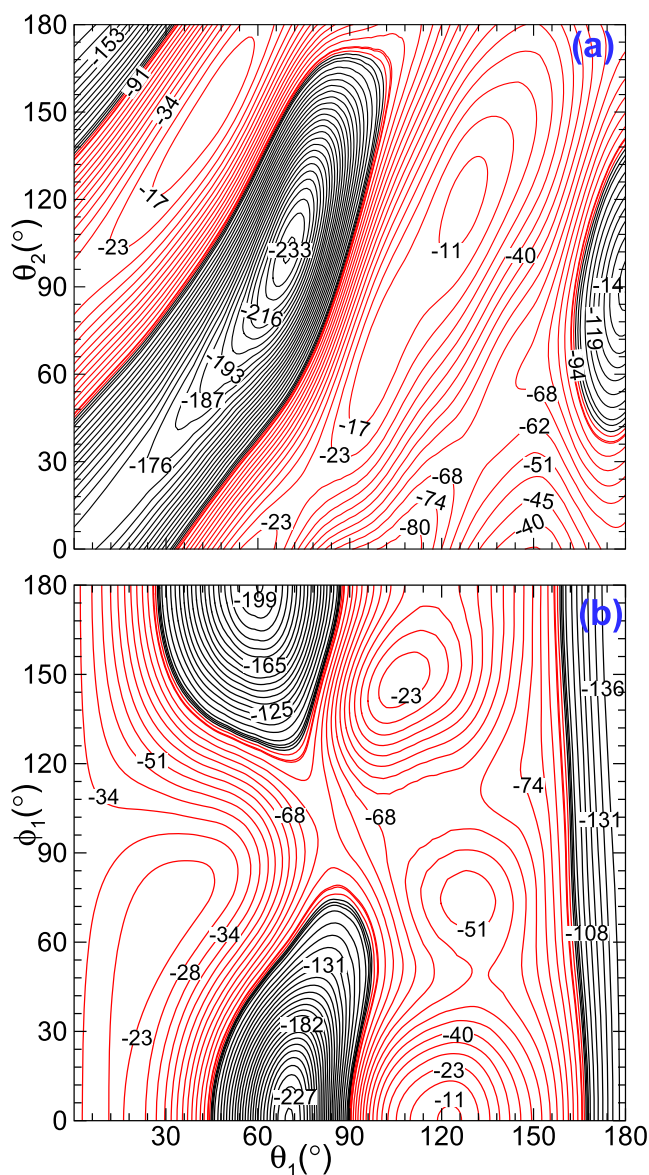


FIG. 4. 2D cut contour plots of our vibrationally averaged 5D V_{MLR} PES for $\text{CH}_3\text{F}(\nu_3=0)-\text{H}_2$: (a) as a function of angles θ_1 and θ_2 and (b) as a function of θ_1 and ϕ_1 with other angular variables fixed at their equilibrium values corresponding to the global minimum, for the optimized value of R .

The Hamiltonian operator for the $\text{CH}_3\text{F}-\text{H}_2$ dimer is reduced to the same form as that for CH_3F interacting with a rare gas atom,

$$\hat{H}_{\text{BO}} = -\frac{\hbar^2}{2\mu} \frac{\partial^2}{\partial R^2} + \frac{(\hat{J} - \hat{j}_{\text{CH}_3\text{F}})^2}{2\mu R^2} + \hat{T}_{\text{CH}_3\text{F}} + V^{\text{AHR}}(R, \theta, \phi), \quad (22)$$

where the subscript “BO” denotes the resemblance to the Born-Oppenheimer treatment of the nuclear vibration problem on an adiabatic electronic PES.

In the angle-averaging process, 16-point Gaussian quadratures were used for integration over both θ_2 and ϕ_2 . Because of symmetry, three even spherical harmonic functions corresponding to $l = 0, 2$, and 4 were used to define $\Psi(\theta_2, \phi_2)$ for $p\text{H}_2$. Here, the AHR coordinate of $\text{CH}_3\text{F}-p\text{H}_2$ is shown in Fig. 1(b), and the AHR effective PES for $\text{CH}_3\text{F}-p\text{H}_2$ was fitted to a 3D MLR form analogous to Eq. (4); full details can be found in Refs. 42 and 43.

In the present work, we employ Eq. (22) to calculate the rovibrational levels of the $\text{CH}_3\text{F}-p\text{H}_2$ complex by using an iterative algorithm, which is based on a parity-adapted basis for symmetry A_1, A_2 , and E . All details of the method can be found in Ref. 41 and references therein. For intermolecular stretching, we used 60 sine discrete variable representation (DVR) grid points from $4.0 a_0$ to $30.0 a_0$, 25 Gaussian-Legendre and 27 Gaussian-Chebyshev quadrature points are used for the numerical integration over θ and ϕ . As discussed in Ref. 41, the eigenfunctions of $\text{CH}_3\text{F}-p\text{H}_2$ can be divided into three symmetry blocks: A_1 (Parity = 0), A_2 (Parity = 1) for *ortho*- $\text{CH}_3\text{F}-p\text{H}_2$ with $\text{mod}(k,3) = 0$, and E for *para*- $\text{CH}_3\text{F}-p\text{H}_2$ species with $\text{mod}(k,3) \neq 0$. k is the projection of j on the C_3 axis of the CH_3F molecule. The transition line strength between two states can be calculated by^{38,43,63}

$$S_{i \rightarrow i'} = 3 \sum_{M, M'} |\langle \Psi_{i'} | \mu_0^{\text{SFF}} | \Psi_i \rangle|^2, \quad (23)$$

where μ_0^{SFF} is the space-fixed Z -component of the dipole moment operator and Ψ_i is the rovibrational wavefunction.

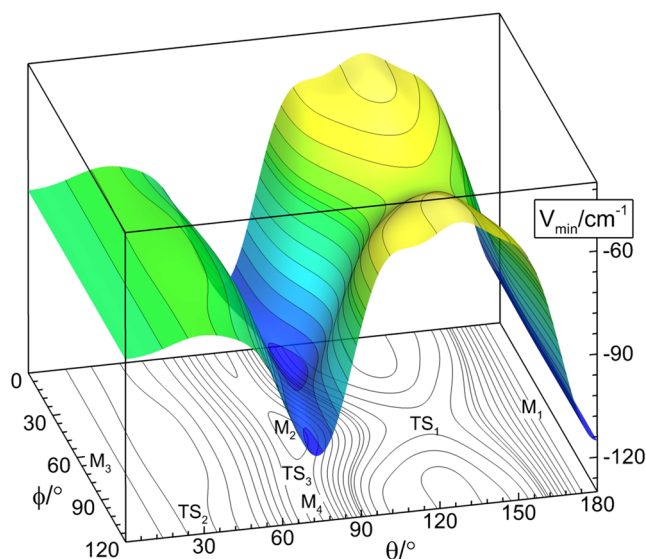


FIG. 5. Minimum energy on the AHR effective 3D PES for $\text{CH}_3\text{F}(\nu_3=0)-p\text{H}_2$ as a function of angles θ and ϕ for the optimized value of R .

TABLE I. Properties of stationary points of the $\text{CH}_3\text{F}(\nu_3 = 0)\text{-pH}_2$ potential energy surface and comparisons with results for previously reported surfaces. All entries are given as $\{R[\text{\AA}], \theta^\circ, \phi^\circ, \bar{V}[\text{cm}^{-1}]\}$, in which some ϕ are given as “...” which means that ϕ can be an arbitrary value from 0.0° to 360.0° .

Species	$\text{CH}_3\text{F-He}^{41}$	$\text{CH}_3\text{F-Ne}^{66}$	$\text{CH}_3\text{F-pH}_2$	$\text{CH}_3\text{F-Ar}^{67}$
Linear (M_1)	{3.83, 180.0, ..., -50.206}	{3.96, 180.0, ..., -86.185}	{3.95, 180.0, ..., -115.052}	{4.25, 180.0, ..., -186.266}
T-shaped (M_2)	{3.07, 84.5, 60.0, -47.544}	{3.16, 84.9, 60.0, -90.556}	{3.17, 82.1, 60.0, -112.798}	{3.45, 83.4, 60.0, -190.807}
Antilinear (M_3)	{3.58, 0.0, ..., -31.492}	{3.66, 0.0, ..., -61.163}	{3.58, 0.0, ..., -76.797}	{3.94, 0.0, ..., -126.789}
T-shaped 2 (M_4)	{3.16, 73.2, 0.0, -43.529}		{3.22, 73.2, 0.0, -110.864}	
TS_1 (M_1 to M_2)	{4.01, 130.1, 60.0, -25.015}	{4.06, 134.4, 60.0, -54.275}	{4.12, 134.9, 60.0, -61.624}	{4.30, 131.1, 60.0, -122.724}
TS_2 (M_3 to M_4)	{3.56, 36.3, 0.0, -26.725}	{3.60, 34.7, 0.0, -55.523}	{3.64, 29.4, 0.0, -72.292}	{3.90, 29.5, 0.0, -120.786}
TS_3 (M_2 to M_4)	{3.15, 76.0, 25.8, -43.021}		{3.24, 76.2, 0.0, -109.368}	

For the $\text{CH}_3\text{F-pH}_2$ dimer, we assume that the dipole moment of the complex is the dipole moment of CH_3F . Assuming that radiation is absorbed by molecules at thermal equilibrium at temperature T , the relative dipole intensity for a transition from a lower state i' to an upper state i is

$$I_{ii'} \propto e^{-E'/k_B T} \times S_{ii'}, \quad (24)$$

where E' is the relative energy of lower state i' .

III. RESULTS AND DISCUSSION

A. Features of the potential energy surface

The global minimum of our vibrationally averaged 5D ground-state PES for $\text{CH}_3\text{F}(\nu_3 = 0)\text{-H}_2$ lies at T-shaped planar geometry ($R = 3.08 \text{ \AA}$, $\theta_1 = 70.4^\circ$, $\theta_2 = 103.2^\circ$, $\phi_1 = \phi_2 = 0^\circ$) with a binding energy of 234.0453 cm^{-1} . In Figs. 3 and 4, we present the 2D cuts (other variables are fixed at their equilibrium values corresponding to the global minimum) of the 5D PES of the $\text{CH}_3\text{F}(\nu_3 = 0)\text{-H}_2$ complex.

In stark contrast to the 5D PES, Fig. 5 displays how the minimum energy surface depends on θ and ϕ with R optimized for AHR effective 3D $\text{CH}_3\text{F-pH}_2$ PES. Since the θ_2 and ϕ_2

degrees of freedom are reduced after the AHR treatment, the term “configuration” only refers to a set of R , θ , and ϕ , and this is different from the discussion of the 5D PES above. As shown in Fig. 5, for the $\text{CH}_3\text{F-pH}_2$ complex, four minima and three transition states are clearly visible; this is consistent with the $\text{CH}_3\text{F-He}$ complex.⁴¹ The global minimum with a well depth of 115.059 cm^{-1} is located at the C end of the C-F bond for the linear geometry ($R = 3.95 \text{ \AA}$, $\theta = 180^\circ$), which is labeled with M_1 . At the F end of the C-F bond, a local minimum with a well depth of 76.797 cm^{-1} occurs at $\theta = 0^\circ$ and $R = 3.58 \text{ \AA}$ for the antilinear geometry, which is referred to as M_3 . Both these two minima lie on the C_3 axis, and there is no energy dependence on angle ϕ . Another two minima were

TABLE II. Calculated $J = 0, 1, 2, 3$ rovibrational energy levels (in cm^{-1}) of the *ortho*- $\text{CH}_3\text{F}(\nu_3)\text{-pH}_2$ complex from our vibrationally averaged 3D AHR PESs with *ortho*- $\text{CH}_3\text{F}(\nu_3)$ at the ground ($\nu_3 = 0$) and first excited ($\nu_3 = 1$) state, separately. D_0 is the dissociation energy, ZPE is the zero-point energy, D_e is the well depth with $D_e = D_0 + \text{ZPE}$, and Δv_0 is the band origin shift.

J	Symmetry	$\nu_3 = 0$	$\nu_3 = 1$	J	Symmetry	$\nu_3 = 0$	$\nu_3 = 1$
0	A_1	-46.445	-47.008	2	A_1	-19.601	-19.965
	A_1	-35.151	-35.419		A_1	-17.918	-18.370
	A_1	-30.703	-31.380		A_1	-16.109	-16.594
	A_1	-20.522	-20.941		A_2	-15.026	-15.508
	A_1	-12.053	-12.606		A_2	-12.760	-13.231
1	A_2	-45.463	-46.030	3	A_1	-12.265	-12.738
	A_2	-44.739	-45.309		A_2	-40.822	-41.404
	A_1	-44.506	-45.077		A_2	-40.415	-40.998
	A_2	-34.542	-34.813		A_1	-39.065	-39.652
	A_2	-29.957	-30.637		A_1	-37.531	-38.129
2	A_2	-24.176	-24.737		A_2	-37.321	-37.918
	A_2	-21.228	-21.577		A_2	-34.351	-34.970
	A_1	-19.360	-19.758		A_1	-34.336	-34.956
	A_2	-17.125	-17.542		A_2	-31.518	-31.804
	A_2	-14.467	-15.005		A_2	-26.085	-26.788
	A_1	-43.558	-44.131		A_2	-20.614	-21.135
	A_1	-42.993	-43.569		A_1	-18.995	-19.620
	A_2	-42.302	-42.880		A_1	-17.811	-18.121
	A_2	-40.511	-41.102		A_2	-17.396	-17.844
	A_1	-40.465	-41.055		A_2	-15.705	-16.076
	A_1	-33.334	-33.610		A_1	-14.182	-14.705
	A_1	-28.401	-29.090		A_2	-13.531	-13.971
	A_1	-22.804	-23.349		D_e	115.059	115.174
	A_2	-22.032	-22.600		ZPE	68.614	68.166
	A_1	-22.804	-23.349		ZPE/ D_e	0.596	0.592
	A_2	-19.994	-20.377		Δv_0	-0.564	

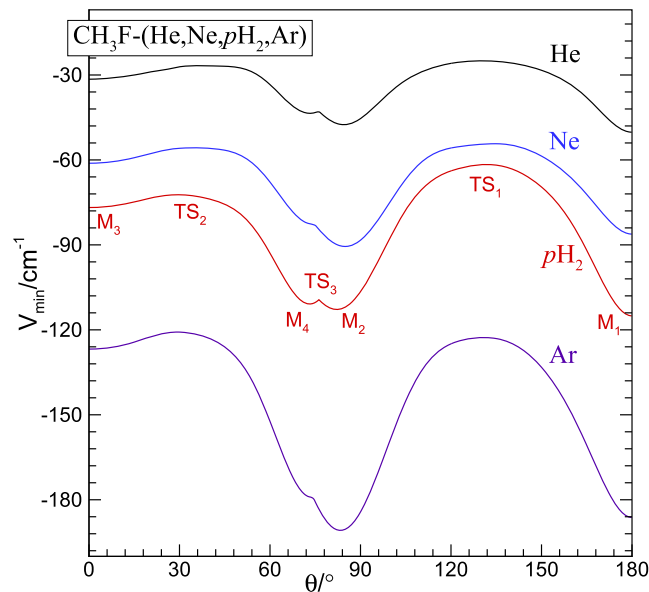


FIG. 6. Minimum energy path for $\text{CH}_3\text{F-pH}_2$ and compared with the $\text{CH}_3\text{F-Rg}$ (He, Ne, Ar) system, as a function of angles θ for the optimized values of R and ϕ .

TABLE III. Calculated $J = 0, 1, 2, 3$ rovibrational energy levels (in cm^{-1}) of the *para*- $\text{CH}_3\text{F}(\nu_3)$ - $p\text{H}_2$ complex from our vibrationally averaged 3D AHR PESs with *para*- $\text{CH}_3\text{F}(\nu_3)$ at the ground ($\nu_3 = 0$) and first excited ($\nu_3 = 1$) state, separately. $\Delta\nu_0$ is the band origin shift.

J	$\nu_3 = 0$	$\nu_3 = 1$	J	$\nu_3 = 0$	$\nu_3 = 1$
0	-40.255	-40.827	2	-36.767	-37.367
	-22.751	-23.332		-34.581	-35.168
	-18.961	-19.494		-31.326	-31.907
	-15.070	-15.486		-28.429	-28.716
	-6.777	-7.245		-24.489	-25.099
1	-40.678	-41.257	3	-23.651	-24.344
	-39.159	-39.738		-22.062	-22.681
	-36.712	-37.287		-36.940	-37.520
	-29.636	-29.916		-35.785	-36.382
	-25.157	-25.844		-34.085	-34.694
2	-24.310	-24.912		-32.389	-33.031
	-21.573	-22.167		-31.288	-31.900
	-18.249	-18.815		-28.154	-28.750
	-39.359	-39.938		-26.651	-26.945
	-38.051	-38.646		-24.584	-25.180
$\Delta\nu_0$	-0.572				

clearly found to be T-shaped structures. One with an energy of 110.864 cm^{-1} is located at ($R = 3.22 \text{ \AA}$, $\theta = 73.2^\circ$, and $\phi = 0^\circ$), which is labeled with M_4 . The other one with an energy of 112.798 cm^{-1} is located at ($R = 3.17 \text{ \AA}$, $\theta = 82.1^\circ$, and $\phi = 60^\circ$), which is labeled with M_2 . The difference between M_2 and M_4 is only 1.934 cm^{-1} , and it is very hard to distinguish between them.

Figure 5 also illustrates how the four minima are connected by three transition states. The first transition state (TS_1) connects the global minimum M_1 and the T-shaped minimum M_2 . It is located at ($R = 4.12 \text{ \AA}$, $\theta = 134.9^\circ$, and $\phi = 60^\circ$) with a barrier of height 61.624 cm^{-1} . The second transition state (TS_2) is connecting the antilinear minimum M_3 and T-shaped minimum M_4 . It is located at ($R = 3.64 \text{ \AA}$, $\theta = 29.4^\circ$, and $\phi = 0^\circ$) with a barrier of height 72.292 cm^{-1} . The last one is referred to TS_3 , which connects the two T-shaped minima of M_2 and M_4 . It is located at ($R = 4.12 \text{ \AA}$, $\theta = 134.9^\circ$, and $\phi = 60^\circ$) with a barrier of height 61.624 cm^{-1} . Table I summarizes the position and the energies of the stationary points of the AHR PES for the $\text{CH}_3\text{F}-p\text{H}_2$ complex and compares with the $\text{CH}_3\text{F}-\text{Rg}$ (He, Ne, Ar) system. As shown in Table I, the stationary points of these PESs are in the same position. However, there

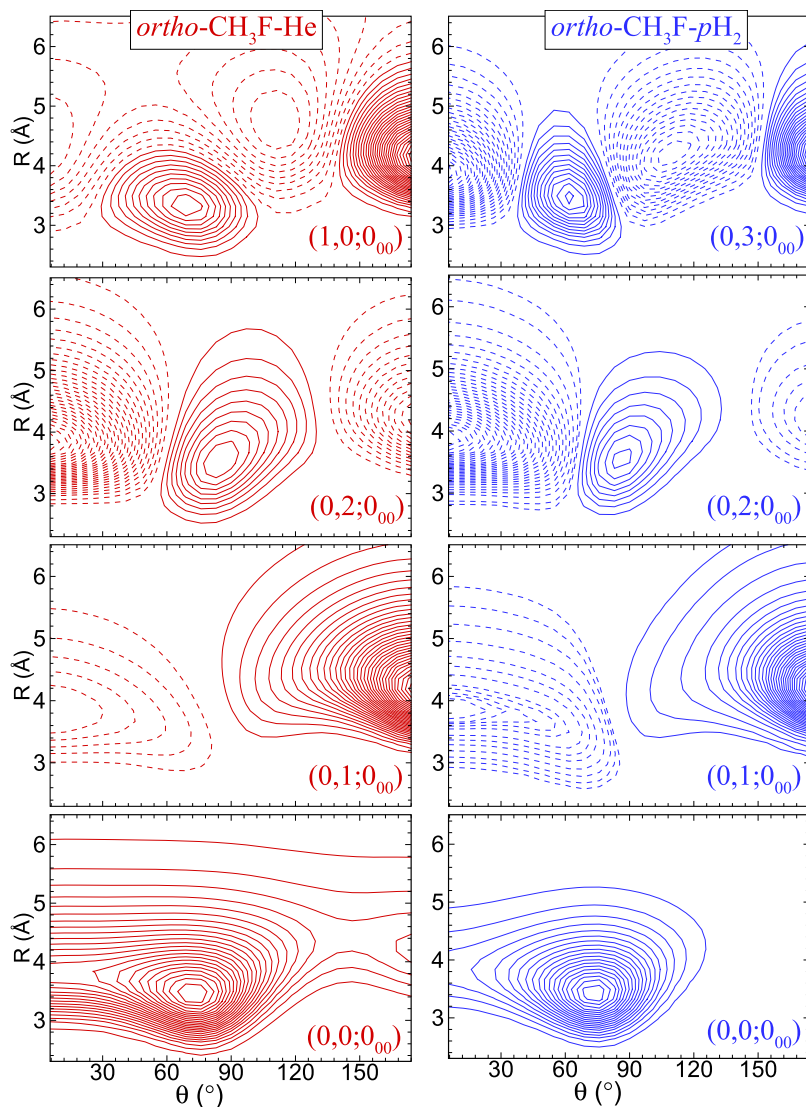


FIG. 7. Wavefunction of the first five rovibration energy levels of the *ortho*- CH_3F -He (left) and *ortho*- CH_3F - $p\text{H}_2$ (right) dimer. The energy levels are labeled with $(n_s, n_b; J_{Ka} Kc)$.

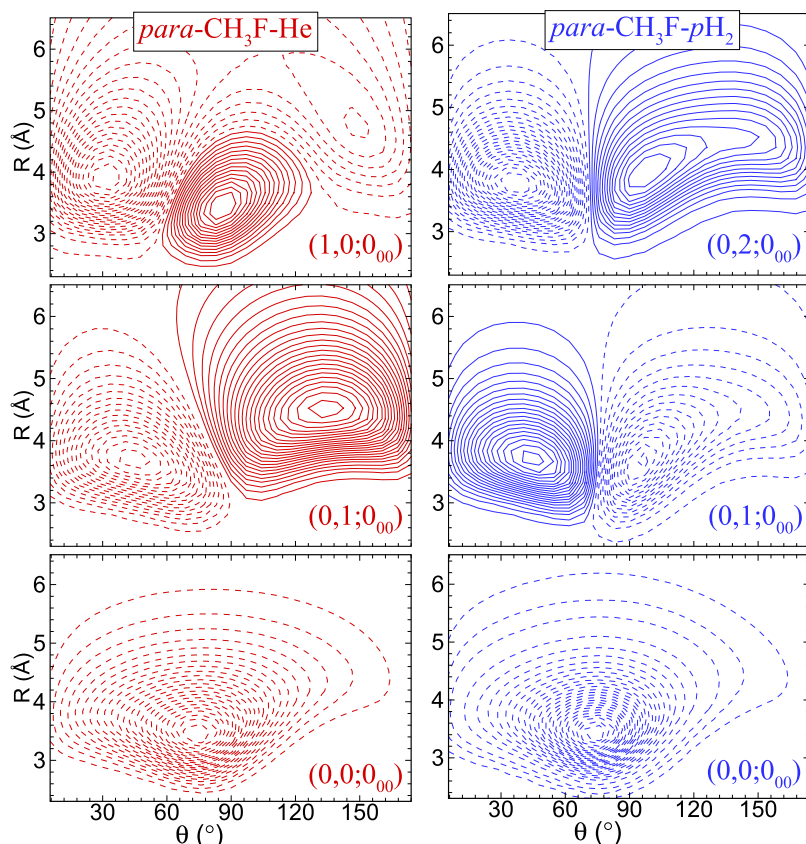


FIG. 8. Wavefunction of the first five rovibration energy levels of the *para*-CH₃F-He (left) and *para*-CH₃F-*p*H₂ (right) dimer. The energy levels are labeled with ($n_s, n_b; J_{K_a} K_c$).

exist large quantitative differences; the T-shaped minima of M₄ for CH₃F-Ne and CH₃F-Ar disappeared. This becomes clear when the minimum potential energy paths are shown in Fig. 6. Although the 1D potential curves along minimum energy paths for CH₃F-Rg (He, Ne, *p*H₂, Ar) are qualitatively similar in shape, differences exist among these three complexes. As we expected, with the increased polarizabilities in the order of He, Ne, *p*H₂, and Ar, the interaction becomes stronger and the well depth becomes deeper for CH₃F-Rg (He, Ne, *p*H₂, Ar). We

noticed that the global minima for CH₃F-Ne and CH₃F-Ar dimers are both located at the T-shaped configuration, while the global minimum of CH₃F-He and CH₃F-*p*H₂ dimers is located at the linear configuration.

B. Bound states and wave functions

The calculated intermolecular rovibrational energy levels for the ground states ($v_3 = 0$) and first excited states ($v_3 = 1$) are listed in Tables II and III for *ortho*-CH₃F-*p*H₂ and *para*-CH₃F-*p*H₂, respectively. As seen in Tables II and III, the calculated bound state energies on the 3D AHR PES ($v_3 = 0$) are about 0.5-2 cm⁻¹ systematically higher than the corresponding values obtained on the 3D AHR PES ($v_3 = 1$) and because our potentials have a shallower well depth. The rovibrational energy levels are labeled by the five quantum numbers n_s, n_b, J, K_a , and K_c , where n_s and n_b are the van der Waals vibrational stretch and bending quantum numbers, and K_a and K_c denote the projections of the total angular momentum J onto the a and c principal axes of inertia.

The zero-point energy (ZPE), difference between the well depth at the potential global minimum ($D_e = |V_{min}|$), and the dissociation energy (D_0) ($ZPE = D_e - D_0$) for *para*- and *ortho*-CH₃F-*p*H₂ complexes are also listed in Tables II and III, as well as the ratios of ZPE/ D_e . The global minimum for CH₃F-*p*H₂ is 64.853 cm⁻¹ deeper than the corresponding values of the CH₃F-He complex, and the ratio (ZPE/ D_e) 2/5 for CH₃F-*p*H₂ is smaller than the 4/5 for CH₃F-He complex, which means that the ground state wave function for *ortho*-CH₃F-*p*H₂ is localized while that for *ortho*-CH₃F-He

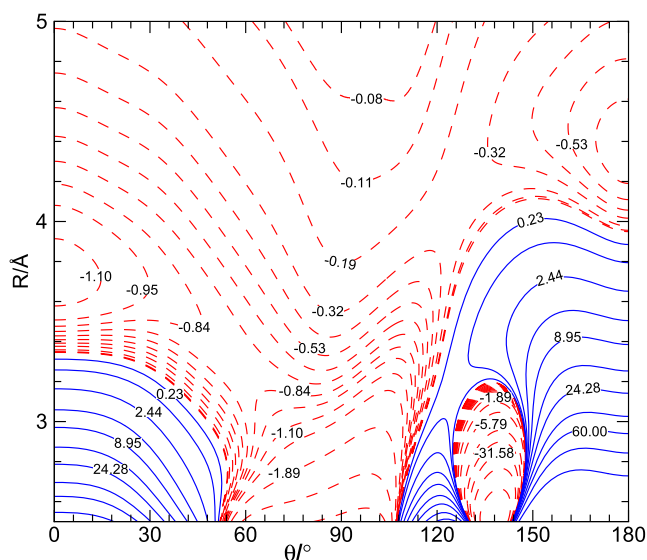


FIG. 9. Difference potential of the AHR 3D CH₃F-*p*H₂ for the $v_3 = 0$ and 1 states as a function of angles θ and R with $\phi = 60^\circ$.

TABLE IV. Predicted rotational transition frequencies (cm^{-1}), line strengths, and relative intensities at a temperature of 2.0 K for the *ortho*-CH₃F-*p*H₂ complex from the 3D AHR PES. The lower and upper states involved in the transitions are numbered with the set of parameters (J , K_a , K_c). The line strength values are multiplied by 1000.

Transitions	V_{MLR}	Line Strength	Intensity (2.0 K)
Lower-upper			
1 ₀₁ -1 ₁₀	0.957	0.297	1.000
1 ₁₁ -2 ₀₂	1.181	0.169	0.338
2 ₂₁ -3 ₃₀	6.175	3.531	0.337
1 ₁₁ -2 ₁₂	1.746	0.078	0.156
1 ₁₁ -1 ₁₀	0.233	0.059	0.119
2 ₂₁ -3 ₂₂	2.980	0.836	0.080
2 ₁₂ -2 ₂₁	2.482	0.137	0.078
2 ₂₁ -2 ₂₀	0.046	0.730	0.070
2 ₁₁ -3 ₁₂	3.238	0.185	0.064
2 ₁₂ -3 ₁₃	2.577	0.104	0.059
1 ₀₁ -2 ₁₂	2.470	0.017	0.056
2 ₀₂ -2 ₁₁	1.256	0.045	0.038
2 ₁₁ -3 ₂₂	4.771	0.100	0.035
2 ₂₁ -3 ₁₂	1.447	0.337	0.032
2 ₁₁ -2 ₂₀	1.837	0.091	0.032
0 ₀₀ -1 ₁₁	1.706	0.003	0.024
2 ₁₂ -3 ₀₃	2.171	0.024	0.014
1 ₁₁ -2 ₂₀	4.274	0.006	0.012
3 ₀₃ -3 ₁₂	1.758	0.044	0.005
2 ₁₂ -2 ₁₁	0.691	0.008	0.004
2 ₀₂ -3 ₁₃	3.142	0.004	0.004
2 ₂₀ -3 ₂₁	3.144	0.029	0.003
1 ₁₀ -2 ₂₁	3.995	0.001	0.001
0 ₀₀ -1 ₀₁	0.982	0.000	0.001
3 ₂₂ -3 ₃₁	3.180	0.078	0.001
2 ₀₂ -3 ₀₃	2.736	0.001	0.001

is delocalized. The wave functions for the first three lowest $J = 0$ energy levels of *ortho*-CH₃F-*p*H₂ are very similar to the *ortho*-CH₃F-He complex, all having clear nodal structures along the θ coordinate, and are localized in the T-shaped, linear, and anti-linear wells, respectively, which is illustrated in Fig. 7. However, the fourth energy for $J = 0$ of *ortho*-CH₃F-He is a stretching mode as evidenced by its node along R . While for the lowest 4 levels of the *ortho*-CH₃F-*p*H₂ complex, there is no node along R . The dissociation energy of *para*-CH₃F-*p*H₂ is 46.289 cm^{-1} corresponding to the $j = |k| = 1$ energy level of CH₃F. This is slightly smaller than the dissociation energy of 46.445 cm^{-1} for the *ortho*-CH₃F-*p*H₂ complex. Therefore, *ortho*-CH₃F-*p*H₂ is more stable than *para*-CH₃F-*p*H₂. In Fig. 8, the wave functions for *para*-CH₃F-*p*H₂ look almost the same as those for the *para*-CH₃F-He complex.

As plotted in Fig. 7, the ground state wave function for *ortho*-CH₃F-*p*H₂ is mainly located at the T-shaped M₂ and M₄ minimum region with a Jacobi angle of $\theta \approx 73^\circ\text{--}85^\circ$ and $R \approx 2.6\text{--}4.2 \text{ \AA}$. In this region, as seen in Fig. 9, the corresponding difference potential of the AHR 3D CH₃F-*p*H₂ for the $\nu_3 = 0$ and 1 states has negative values. This explains why the predicted ν_3 vibrational frequency shift is red shift. The same result can be obtained by analyzing the ground state wave function and the difference potential for the *para*-CH₃F-*p*H₂ complex. As shown in the last rows of Tables II and III, the calculated band origin shifts predicted on our 3D

TABLE V. Predicted rotational transition frequencies (cm^{-1}), line strengths, and relative intensities at a temperature of 2.0 K for the *para*-CH₃F-*p*H₂ complex from the 3D AHR PES. The lower and upper states involved in the transitions are numbered with the set of parameters (J , K_a , K_c). The line strength values are multiplied by 100.

Transitions	V_{MLR}	Line Strength	Intensity (2.0 K)
Lower-upper			
2 ₀₂ -2 ₁₂	1.309	2.175	1.000
1 ₀₁ -1 ₁₁	1.520	0.540	0.641
1 ₁₁ -1 ₁₀	2.447	1.252	0.498
3 ₀₃ -3 ₁₃	1.154	2.807	0.226
2 ₁₂ -2 ₁₁	1.284	1.224	0.220
2 ₁₁ -2 ₂₁	2.186	1.679	0.120
2 ₀₂ -2 ₁₁	2.592	0.225	0.104
2 ₁₂ -2 ₂₁	3.470	0.434	0.078
3 ₀₃ -3 ₁₂	2.855	0.554	0.045
3 ₁₂ -3 ₂₂	1.696	2.071	0.021
3 ₁₃ -3 ₁₂	1.701	0.392	0.014
2 ₂₁ -2 ₂₀	3.255	0.833	0.012
3 ₁₂ -3 ₂₁	2.796	0.999	0.010
2 ₁₁ -2 ₂₀	5.441	0.025	0.002
3 ₁₃ -3 ₂₂	3.396	0.050	0.002
3 ₂₁ -3 ₃₁	3.135	0.649	0.001

AHR surfaces are $\Delta v_0 = -0.572 \text{ cm}^{-1}$ for *para*-CH₃F-*p*H₂ and -0.564 cm^{-1} for *ortho*-CH₃F-*p*H₂, respectively. Both are red shifts, and they are in the same order of magnitude from the estimated value of -0.70 cm^{-1} (average shift per *p*H₂ molecule) and -0.71 cm^{-1} (difference between the vibrational shift for CH₃F solvated by one *o*H₂ and 11 *p*H₂ molecules and by 12 nearest neighbor *p*H₂ molecules).¹⁰ The predicted shifts will provide valuable information for future infrared spectrum studies on the CH₃F-H₂ dimer or CH₃F-(*p*H₂)_N clusters.

C. Predicted microwave and infrared transitions

For *ortho*-CH₃F-*p*H₂, the predicted microwave (MW) transitions, line strength, and relative intensities at temperature 2.0 K are listed in Table IV. The lower and upper states involved in the transitions are numbered with the set of parameters (J , K_a , K_c). Note that the line strength does not depend on the temperature. Subject to the selection rules $\Delta J = 0, \pm 1$ and the approximate ones of $\Delta j = 0, \pm 1$, $\Delta l = 0$,⁶⁴ a total of 72 possible transitions for $J \leq 3$ are predicted. To select the most possible MW transitions, we only reported relative intensity ≥ 0.001 . As shown in Table IV, all relative intensity is calculated relative to 1₀₁-1₁₀ transition, whose intensity is set to 1.

For *para*-CH₃F-*p*H₂, the predicted microwave (MW) transitions, line strength, and relative intensities at temperature 2.0 K are listed in Table V. A total of 102 possible transitions for $J \leq 3$ are predicted. Similarly, we only listed the most possible transitions and the ones relative to 2₀₂-2₁₂ transition. Figure 10 shows the line strength and relative intensities at 2.0 K for *ortho*-CH₃F-*p*H₂ and *para*-CH₃F-*p*H₂, respectively. Most of the relative intensities are reduced; however, for *ortho*-CH₃F-*p*H₂, the transitions of 1₀₁-1₁₁, 1₁₁-2₀₂, and 2₂₁-3₃₀ and, for *para*-CH₃F-*p*H₂, the transitions of 2₀₂-2₁₂,

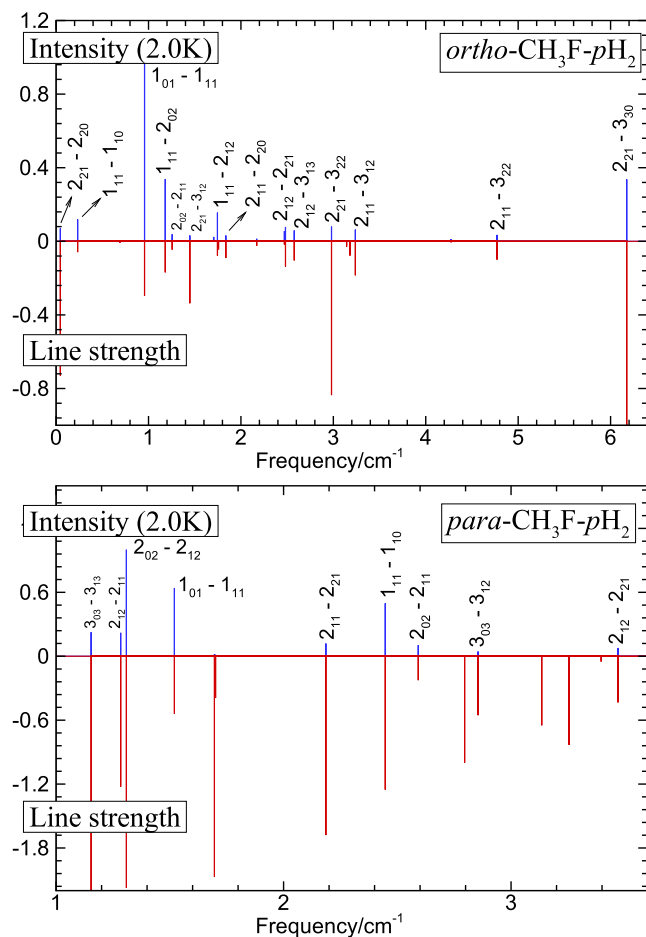


FIG. 10. Calculated rotational spectra (labeled with $J_{K_a K_c}$) of *ortho*-CH₃F-*p*H₂ and *para*-CH₃F-*p*H₂, shown with line strengths (downward pointing lines) and relative intensities at 2 K (upward pointing lines), respectively.

$1_{01}-1_{11}$, and $1_{11}-1_{10}$ still have very high intensities. This finding can provide useful information for future assignment of experimental spectra of the *ortho/para*-CH₃F-*p*H₂ dimer at ultra-cold temperature.

For *ortho*-CH₃F-*p*H₂ and *para*-CH₃F-*p*H₂, infrared (IR) $\nu_3 = 0 \rightarrow 1$ transition frequencies calculated from our 3D V_{MLR} are listed in Tables S-I and S-II of the [supplementary material](#). All the infrared transition energies are relative the C-F stretching vibrational frequency of the free CH₃F molecule (fixed at the experimental value of 1048.611 cm⁻¹).⁶⁵

IV. CONCLUSIONS

We have presented an accurate analytic vibrationally averaged 5D potential energy surface for CH₃F(ν_3)-H₂ complexes for $\nu_3 = 0$ and $\nu_3 = 1$ which was obtained from six-dimensional *ab initio* potential energies. The PESs explicitly incorporate the Q_3 normal-mode coordinate of the CH₃F molecule. The *ab initio* interaction energies were obtained at the CCSD(T)-F12a level of theory using the aVTZ basis set. The vibrationally averaged potential energies were first fitted to a 5D MLR potential form that incorporates the theoretically known long-range inverse-power. We have thus shown that the corresponding 5D fit of the CH₃F(ν_3)-H₂ surface provides for the first time an accuracy of about 0.74 cm⁻¹ and 0.082 cm⁻¹ in

the van der Waals minimum region of the interaction. It was found from the calculations that the global minimum of the 5D PES corresponds to a structure with intermolecular separation $R = 3.08$ Å and $\theta_1 = 70.3^\circ$, $\theta_2 = 102.9^\circ$, $\phi_1 = \phi_2 = 0^\circ$ with a binding energy of 234.0418 cm⁻¹. Full five dimensions are currently under way for the CH₃F(ν_3)-H₂ complex. In this context, we note that spectra of solid *p*H₂ doped with CH₃F experiments have been carried out very recently.

The adiabatic-hindered-rotor approximation was then used to average over H₂ orientations to obtain effective 3D PESs for the CH₃F-*p*H₂ complex. This approximation is based on the assumption that the *p*H₂ rotation is much faster than the motions of other degrees of freedom and can therefore be adiabatically separated out. It reduces the dimension of the original rigid-rotor CH₃F(ν_3)-H₂ potential from 5D to 3D and leads to a substantial reduction in computational effort. The 3D AHR PES for CH₃F-*p*H₂ shows striking differences from the original 5D potential. In particular, the original global minimum disappears, and the new global minimum is located at the C end of C-F bond for the linear geometry. This 3D AHR PES has been employed in the computation of the rovibrational energy level for *para*- and *ortho*-CH₃F-H₂ complexes and predicts the IR and microwave spectra for the first time. Exact wave functions with a clear nodal structure and contour plots are also obtained and used to analyze the average structures, properties, and transition line strengths. Since the 3D AHR PES is associated with the fundamental transition of ν_3 (CH₃F), the calculated infrared spectra and band origin shifts for *para*-CH₃F-H₂ and *ortho*-CH₃F-H₂ dimers are also reported for the first time, which will serve as a good starting point and provide reliable guidance for future studies of CH₃F doped in H₂ clusters.

SUPPLEMENTARY MATERIAL

See [supplementary material](#) for the FORTRAN subroutine of the vibrationally averaged 5D- V_{MLR} PESs for the CH₃F-H₂ complex and Tables SI and SII, which present the predicted infrared transition frequencies, line strengths, and relative intensities of *ortho*-CH₃F-*p*H₂ and *para*-CH₃F-*p*H₂.

ACKNOWLEDGMENTS

This research has been supported by the National Key Research and Development Program (Grant Nos. 2017YFB0203401 and 2016YFB0700801) and the National Natural Science Foundation of China (Grant Nos. 21773081, 21533003, and 91541124). X.-L.Z. also would like to acknowledge financial support from the China Scholarship Council (Grant No. 201500090191).

¹J. Van Kranendonk, *Solid Hydrogen* (Plenum, New York, 1983).

²T. Oka, *Annu. Rev. Phys. Chem.* **44**, 299 (1993).

³T. Momose and T. Shida, *Bull. Chem. Soc. Jpn.* **71**, 1 (1998).

⁴M. E. Fajardo and S. Tam, *J. Chem. Phys.* **108**, 4237 (1998).

⁵T. Momose, H. Hoshina, M. Fushitani, and H. Katsuki, *Vib. Spectrosc.* **34**, 95 (2004).

⁶M. E. Fajardo, C. M. Lindsay, and T. Momose, *J. Chem. Phys.* **130**, 244508 (2009).

⁷Y.-P. Lee, Y.-J. Wu, R. M. Lees, L.-H. Xu, and J. T. Hougen, *Science* **311**, 365 (2006).

- ⁸S. Tam, M. E. Fajardo, H. Katsuki, H. Hoshina, T. Wakabayashi, and T. Momose, *J. Chem. Phys.* **111**, 4191 (1999).
- ⁹T. Momose, M. Miki, T. Wakabayashi, T. Shida, M.-C. Chan, S. S. Lee, and T. Oka, *J. Chem. Phys.* **107**, 7707 (1997).
- ¹⁰K. Yoshioka and D. T. Anderson, *J. Chem. Phys.* **119**, 4731 (2003).
- ¹¹K. Yoshioka and D. T. Anderson, *J. Mol. Spectrosc.* **786**, 123 (2006).
- ¹²Y.-P. Lee, Y.-J. Wu, and J. T. Hougen, *J. Chem. Phys.* **129**, 104502 (2008).
- ¹³Y. Miyamoto, T. Momose, and H. Kanamori, *J. Chem. Phys.* **137**, 194315 (2012).
- ¹⁴A. McKellar, A. Mizoguchi, and H. Kanamori, *Phys. Chem. Chem. Phys.* **13**, 11587 (2011).
- ¹⁵A. McKellar, A. Mizoguchi, and H. Kanamori, *J. Chem. Phys.* **135**, 124511 (2011).
- ¹⁶H. Kawasaki, A. Mizoguchi, and H. Kanamori, *J. Mol. Spectrosc.* **310**, 39 (2015).
- ¹⁷H. Kawasaki, A. Mizoguchi, and H. Kanamori, *J. Chem. Phys.* **144**, 184306 (2016).
- ¹⁸Y. Miyamoto, A. Mizoguchi, and H. Kanamori, *J. Chem. Phys.* **146**, 114302 (2017).
- ¹⁹S. C. Althorpe and D. C. Clary, *J. Chem. Phys.* **101**, 3603 (1994).
- ²⁰E. H. T. Olthof, A. van der Avoird, and P. E. S. Wormer, *J. Chem. Phys.* **101**, 8430 (1994).
- ²¹C. Leforestier, F. Gatti, R. S. Fellers, and R. J. Saykally, *J. Chem. Phys.* **117**, 8710 (2002).
- ²²G. C. Groenenboom, P. E. S. Wormer, A. van der Avoird, E. M. Mas, R. Bukowski, and K. Szalewicz, *J. Chem. Phys.* **113**, 6702 (2000).
- ²³R. Bukowski, K. Szalewicz, G. C. Groenenboom, and A. van der Avoird, *Science* **315**, 1249 (2007).
- ²⁴X. Huang, B. J. Braams, J. M. Bowman, R. E. A. Kelly, J. Tennyson, G. C. Groenenboom, and A. van der Avoird, *J. Chem. Phys.* **128**, 034312 (2008).
- ²⁵M. J. Smit, G. C. Groenenboom, P. E. S. Wormer, A. van der Avoird, R. Bukowski, and K. Szalewicz, *J. Phys. Chem. A* **105**, 6212 (2001).
- ²⁶A. N. Panda, F. Otto, F. Gatti, and H.-D. Meyer, *J. Chem. Phys.* **127**, 114310 (2007).
- ²⁷F. Otto, F. Gatti, and H.-D. Meyer, *J. Chem. Phys.* **128**, 064305 (2008).
- ²⁸T. R. Phillips, S. Maluendes, A. D. McLean, and S. Green, *J. Chem. Phys.* **101**, 5824 (1994).
- ²⁹P. Valiron, M. Wernli, A. Faure, L. Wiesenfeld, C. Rist, S. Kedžuch, and J. Noga, *J. Chem. Phys.* **129**, 134306 (2008).
- ³⁰N. S. Dattani and R. J. Le Roy, *J. Mol. Spectrosc.* **268**, 199 (2011).
- ³¹Y. Zhai, H. Li, and R. J. Le Roy, *Mol. Phys.* **1** (2018).
- ³²R. J. Le Roy, N. S. Dattani, J. A. Coxon, A. J. Ross, P. Crozet, and C. Linton, *J. Chem. Phys.* **131**, 204309 (2009).
- ³³L. Wang, D. Q. Xie, R. J. Le Roy, and P.-N. Roy, *J. Chem. Phys.* **137**, 104311 (2012).
- ³⁴H. Li and R. J. Le Roy, *Phys. Chem. Chem. Phys.* **10**, 4128 (2008).
- ³⁵H. Li, X.-L. Zhang, R. J. Le Roy, and P.-N. Roy, *J. Chem. Phys.* **139**, 164315 (2013).
- ³⁶L. Wang, D. Q. Xie, R. J. Le Roy, and P.-N. Roy, *J. Chem. Phys.* **139**, 034312 (2013).
- ³⁷H. Li, P.-N. Roy, and R. J. Le Roy, *J. Chem. Phys.* **132**, 214309 (2010).
- ³⁸J.-M. Liu, Y. Zhai, and H. Li, *J. Chem. Phys.* **147**, 044313 (2017).
- ³⁹J.-M. Liu, Y. Zhai, X.-L. Zhang, and H. Li, *Phys. Chem. Chem. Phys.* **20**, 2036 (2018).
- ⁴⁰D. Hou, Y.-T. Ma, X.-L. Zhang, and H. Li, *J. Chem. Phys.* **144**, 014301 (2016).
- ⁴¹Y.-T. Ma, T. Zeng, and H. Li, *J. Chem. Phys.* **140**, 214309 (2014).
- ⁴²H. Li, P.-N. Roy, and R. J. Le Roy, *J. Chem. Phys.* **133**, 104305 (2010).
- ⁴³T. Zeng, H. Li, R. J. Le Roy, and P.-N. Roy, *J. Chem. Phys.* **135**, 094304 (2011).
- ⁴⁴R. J. Le Roy and J. M. Hutson, *J. Chem. Phys.* **86**, 837 (1987).
- ⁴⁵G. Knizia, T. B. Adler, and H.-J. Werner, *J. Chem. Phys.* **130**, 054104 (2009).
- ⁴⁶T. H. Dunning, Jr., *J. Chem. Phys.* **90**, 1007 (1989).
- ⁴⁷H.-J. Werner, P. J. Knowles, G. Knizia, F. R. Manby, M. Schütz *et al.*, MOLPRO, version 2012.1, a package of *ab initio* programs, 2012, see <http://www.molpro.net>.
- ⁴⁸S. F. Boys and F. Bernardi, *Mol. Phys.* **19**, 553 (1970).
- ⁴⁹H. Wei and T. Carrington, Jr., *J. Chem. Phys.* **97**, 3029 (1992).
- ⁵⁰J. Echave and D. C. Clary, *Chem. Phys. Lett.* **190**, 225 (1992).
- ⁵¹R. J. Le Roy and R. D. E. Henderson, *Mol. Phys.* **105**, 663 (2007).
- ⁵²T. N. Olney, N. M. Cann, G. Cooper, and C. E. Brion, *Chem. Phys.* **223**, 59 (1997).
- ⁵³H. Li and R. J. Le Roy, *J. Chem. Phys.* **126**, 224301 (2007).
- ⁵⁴H. D. Cohen and C. C. J. Roothaan, *J. Chem. Phys.* **43**, S34 (1965).
- ⁵⁵D. M. Bishop and L. M. Cheung, *J. Chem. Phys.* **72**, 5125 (1980).
- ⁵⁶R. J. Le Roy and A. Pashov, *J. Quant. Spectrosc. Radiat. Transfer* **186**, 210 (2017).
- ⁵⁷G. Brocks, A. van der Avoird, B. Sutcliffe, and J. Tennyson, *Mol. Phys.* **50**, 1025 (1983).
- ⁵⁸F. Gatti and C. Iung, *Phys. Rep.* **484**, 1 (2009).
- ⁵⁹X.-G. Wang and T. Carrington, Jr., *J. Chem. Phys.* **134**, 044313 (2011).
- ⁶⁰A. van der Avoird and D. J. Nesbitt, *J. Chem. Phys.* **134**, 044314 (2011).
- ⁶¹D. Papoušek, Y.-C. Hsu, H.-S. Chen, P. Pracna, S. Klee, and M. Winniewisser, *J. Mol. Spectrosc.* **159**, 33 (1993).
- ⁶²D. Papoušek, J. Demaison, G. Włodarczak, P. Pracna, S. Klee, and M. Winniewisser, *J. Mol. Spectrosc.* **164**, 351 (1994).
- ⁶³J. M. Hutson, *J. Chem. Phys.* **92**, 157 (1990).
- ⁶⁴A. R. W. McKellar, *J. Chem. Phys.* **108**, 1811 (1998).
- ⁶⁵S. Freund, G. Duxbury, M. Römhild, J. Tiedje, and T. Oka, *J. Mol. Spectrosc.* **52**, 38 (1974).
- ⁶⁶Y.-T. Ma, Y.-Y. Zhao, D. Hou, and H. Li, *Chem. Res. Chin. Univ.* **32**, 818 (2016).
- ⁶⁷Y.-T. Ma and H. Li, *Sci. Sin.: Chim.* **45**, 1345 (2015).